Materials Advances

ROYAL SOCIETY OF CHEMISTRY

Check for updates

Enhanced energy storage properties of red phosphorus/black phosphorus hybrid nanostructures

Shahbaz Ahmad and Mohd Zubair Ansari [ID] *

The systematic investigation of the synthesis and characterisation of black phosphorus (BP) and red phosphorus (RP) hybrids was conducted to delve into their structural, morphological, and electrochemical properties. The phase transformation of amorphous RP to crystalline orthorhombic BP was achieved through a solvothermal approach, as confirmed by X-ray diffraction (XRD) and Raman spectroscopy. A complete phase transition was observed at 200 °C, with lattice parameters measured as a = 3.311 Å, b = 10.421 Å, and c = 4.373 Å. Additionally, Raman analysis identified characteristic BP vibrational modes at 361.62, 443.22, and 468.56 cm^{-1}. The crystalline nature of BP was confirmed through transmission electron microscopy (TEM) and selected area electron diffraction (SAED), revealing lattice fringes that correspond to the (111), (151) and (060) planes with a spacing of 0.245 nm, 0.166 nm and 0.176 nm. The analyses conducted through SEM and EDX demonstrated a layered structure devoid of impurities. The BET surface area analysis indicated a notable enhancement for the BP/RP hybrid, measuring 29.30 m^2 g^{-1}, in contrast to pristine BP at 16.27 m^2 g^{-1} and RP at 3.86 m^2 g^{-1}. The electrochemical characterisation revealed the exceptional pseudocapacitive performance of the BP/RP hybrid, attaining a high specific capacitance of 87 F g^{-1} at 0.5 A g^{-1}, surpassing values documented for comparable systems.

1. Introduction

The rapid growth of portable electronic devices, coupled with an increasing demand for sustainable energy solutions, has led to a heightened interest in supercapacitors[1–3] and in hybrid electrode materials.[4,5] Transition metal phosphides, layered hydroxides, and carbon-based composites have demonstrated promising potential owing to their high theoretical capacitance, structural tunability, and excellent conductivity.[6,7] Recent advances in defect engineering, heterostructure construction, and morphology control—such as phosphorus vacancy regulation or template-derived nanostructures—further enhance charge transfer kinetics and electrochemical stability.[8] These devices are recognised for their superior characteristics, including rapid charge and discharge capabilities, extended cycle longevity, and elevated power density when compared to traditional energy-storage systems like dielectric capacitors and lithium-ion batteries.[9,10] In general, the attainment of elevated capacitance in electrical double-layer capacitors (EDLCs) necessitates the presence of substantial specific surface areas in electrode materials, as this phenomenon arises from the electrosorption of ions onto the electrodes.[6–8] Layered materials exhibit significant potential as electrode materials in electrochemical energy-storage devices, where the efficient intercalation of ions is crucial.[11,12]

Recently, black phosphorus (BP), a thermodynamically stable allotrope of phosphorus,[13] has gained significant attention due to its layered structure,[2,14] similar to graphite, held together by van der Waals forces.[11] This structure grants BP exceptional electronic and optical properties,[15] making it suitable for electronic, optoelectronic, and energy-storage applications.[16–19] With a high theoretical specific capacity and carrier mobility,[20,21] BP is a promising electrode material for lithium-ion batteries,[13,22] offering an initial charge capacity of 1279 mAh g^{-1}, though it drops to 220 mAh g^{-1} after 30 cycles.[23] BP has also been used in flexible supercapacitors,[24] achieving a specific capacitance of 45.8 F g^{-1} at 10 mV s^{-1}.[25] Traditionally, BP is synthesized from white phosphorus under high pressure and temperature.[26] Methods like chemical vapor transport (CVT),[27] bismuth flux,[28] and mercury catalysis[29] produce high-quality crystals but are energy-intensive, yield-limited, or involve hazardous materials.[13] Recent advancements include low-pressure, non-toxic methods using mineralisers and high-energy mechanical milling (HEMM) at ambient conditions.[30,31] Sonochemistry has also enabled large-scale BP production, though it requires high temperature and pressure.[21] Recently, solvothermal synthesis has emerged as a cost-effective and scalable method for producing BP in typical lab settings.[14,32,33] Using ethylenediamine (ED) as a stable and

Department of Physics, National Institute of Technology Srinagar, Hazratbal, Srinagar, Jammu and Kashmir, 190006, India. E-mail: mhd.zubair1@gmail.com

eco-friendly medium, this approach transforms red phosphorus (RP) into BP under controlled temperature and pressure.[13,32] While RP shares a comparable theoretical capacity with BP, its poor conductivity and volume changes during cycling hinder performance.[34] Incorporating BP into the RP matrix creates a heterostructure with excellent interfacial contact,[35] enhancing electron transport and leveraging BP's superior charge carrier mobility.[34] This method avoids the drawbacks of carbon-based conductive additives, which can reduce capacity, making BP a promising alternative for improving electrochemical performance.[36]

This work methodically investigates the solvothermal synthesis of black phosphorus (BP) derived from red phosphorus (RP), emphasizing the structural transformations, morphological changes, and electrochemical behaviour of the resulting nanostructures.

2. Synthesis method

Red phosphorus (RP), ethylenediamine (ED), ethanol, acetone, and deionised water were all acquired for the study. A schematic representation of the synthesis procedure is depicted in Fig. 1, where BP nanosheets were synthesised using a direct solvothermal method, with ethylenediamine serving as the solvent and red phosphorus acting as the precursor material. In a standard synthesis procedure, 2 g of red phosphorus was combined with 70 mL of ethylenediamine. Following a 30-minute period of vigorous agitation, the resulting mixture was placed into a 100 mL Teflon-lined stainless-steel autoclave, where it underwent thermal treatment at a temperature ranging from 120–200 °C for 24 hours. After undergoing a natural cooling process to achieve

ambient temperature, the product was then gathered and treated with rinses of ethanol and acetone. The final product underwent an overnight drying process at a temperature of 70 °C.

Prior to the application of the slurry comprising RP and ED, the purchased RP experienced oxidation as a consequence of its interaction with water and oxygen. This process led to the formation of phosphate groups on its surface, which impeded its solubility in ED. In order to mitigate the oxidation, the RP underwent hydrothermal treatment within a 100 mL Teflon-lined stainless-steel autoclave for a period of 24 hours at a temperature of 160 °C.

3. Characterizations

The synthesized BP and BP/RP hybrid nanostructures were characterized using a Smart Lab 3 kW X-ray diffractometer from Rigaku for X-ray diffraction (XRD), the Raman spectra of the synthesised nanostructures were meticulously recorded utilising a Renishaw Raman microscope, and scanning electron microscopy (SEM) and energy dispersive X-ray (EDX) spectroscopy were performed using a Hitachi 3600 N Scanning electron microscope with a 5 axis motorized stage coupled with an ultra-dry Compact EDS Detector at the Central Research Facility Centre (CRFC) of NIT Srinagar. A Nexsa-Thermo-fisher spectrometer, utilising monochromatized Al Kα radiation, was employed to conduct X-ray photoelectron spectroscopy (XPS) for the analysis of the oxidation states of the materials. The XPS peaks were deconvoluted utilising the XPSPEAK41 software. Transmission electron microscopy (TEM), named as the Tecnai G2 20 S-TWIN [FEI] is a 200 KeV TEM designed to offer high-resolution imaging high-resolution TEM (HR-TEM) accompanied by the selected area
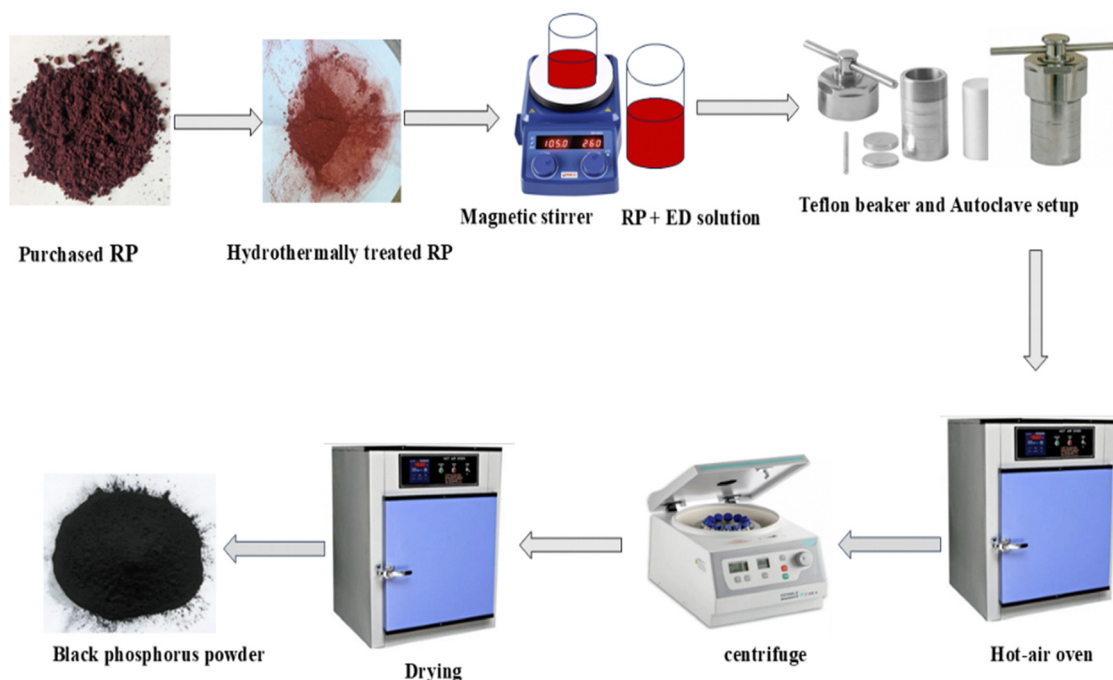

Fig. 1 Schematic diagram of solvothermal synthesis of BP from RP.

electron diffraction (SAED) patterns offer profound insights into the morphology, structural characteristics, and crystallinity. Surface area was measured *via* Brunauer–Emmett–Teller (BET) analysis using a Nova Touch LX2 gas adsorption analyser from Quanta Chrome Instruments. Electrochemical properties were evaluated through cyclic voltammetry (CV), galvanostatic charge–discharge (GCD), and electrochemical impedance spectroscopy (EIS) using a Bio-Logic SP-200 workstation.

4. Results and discussion

4.1. X-ray diffraction pattern analysis of the synthesized nanostructures

Fig. 2(a) shows the XRD patterns of RP, BP-120, BP-140, BP-160, BP-180 and BP-200. The XRD profiles fully agree with previous reports.[14,33,37] The XRD patterns demonstrate the conversion of RP to BP as a function of synthesis temperature spanning from 120 °C to 200 °C, with 20 °C increments between successive synthesis stages. At 120 °C, a minor residual RP phase persists,[33] as denoted by the peak marked with an asterisk (*). With the rise in temperature, there is a notable reduction in the intensity of this peak, indicating that both synthesized samples exhibit RP/BP heterostructures,[35] where the orthorhombic phase emerges as the dominant configuration. At 160 °C, the RP peak is entirely absent, thereby confirming the phase transition to orthorhombic BP. Subsequent increases in temperature enhance the crystallinity of the peaks related to the orthorhombic phase.[13] The phase transformation of red phosphorus (RP) to black phosphorus (BP) proceeds *via* a multi-step process involving molecular activation, intermediate formation, and directional crystal growth, facilitated by solvent interactions and thermal energy. In this work, gram-scale BP was synthesized using a recyclable, low-temperature liquid-phase method employing ethylenediamine (ED) as both the solvent and activator, at temperatures ranging from 120 to 200 °C. The transformation mechanism begins with the activation of the P_4 tetrahedral units of RP by ED molecules through electron transfer from the highest occupied molecular orbital (HOMO) of ED (electron donor) to the lowest unoccupied molecular orbital (LUMO) of P_4 (electron acceptor).[13,35] This electronic interaction induces bond asymmetry within the P_4 cluster, producing two short P–P bonds and one elongated P–P bond. Subsequently, two activated P_4 units couple symmetrically to form a stable P_8 basic unit, which serves as the structural nucleus for crystal growth. The growth of BP follows a spatially directed pathway: initial extension occurs along the *x*-axis, driven by the short P–P bonds, followed by growth along the *y*-axis, mediated by the relatively weaker long P–P bonds. Final stacking and ordering along the *z*-axis are facilitated by van der Waals (VDW) interactions,[38]
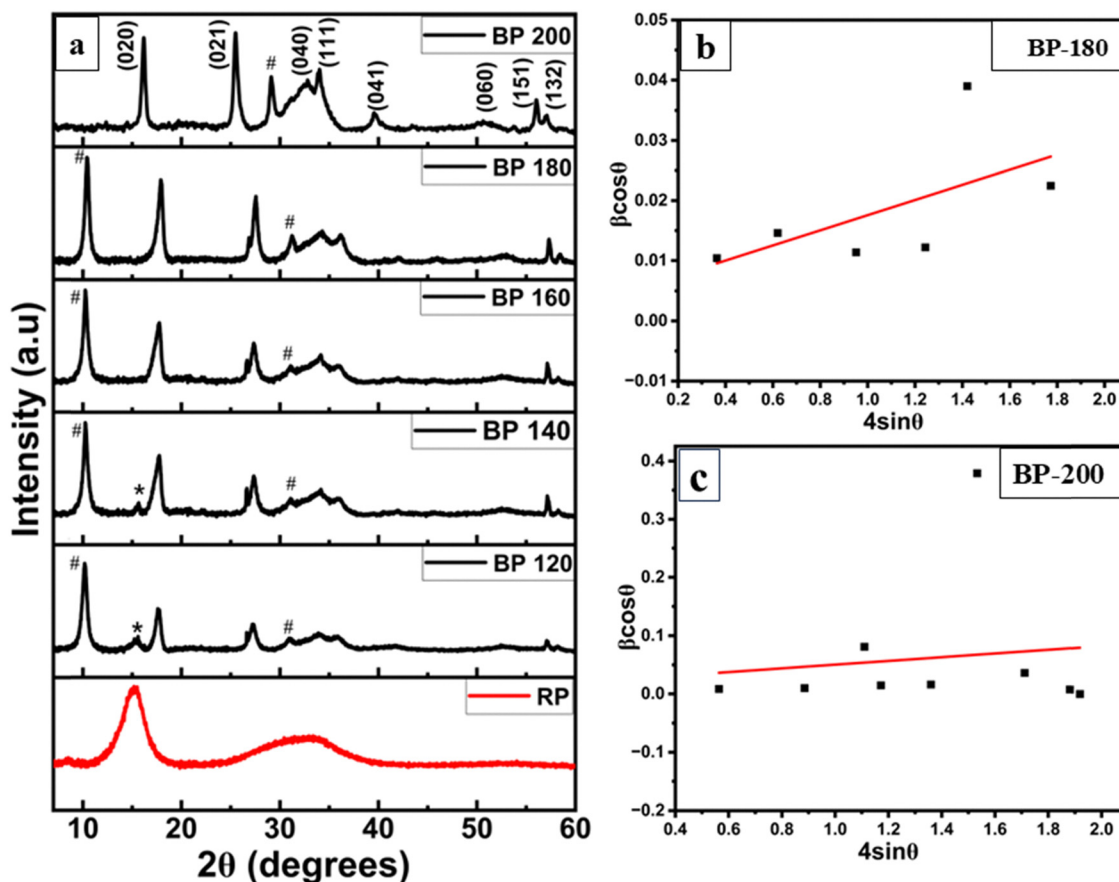

Fig. 2   (a) XRD patterns of RP, BP-120, BP-140, BP-160, BP-180 and BP-200. (b) and (c) W–H plots of BP-180 and BP-200, respectively.

Table 1 Miller indices (*hkl*) and Bragg angles (2θ°) of BP synthesized at 200 °C and 180 °C

Miller indices (*hkl*)	(020)	(021)	(040)	(111)	(041)	(060)	(151)	(132)
BP-180 °C	17.81	27.40	34.19	36.15	42.09	52.93	57.34	56.39
BP-200 °C	16.20	25.51	32.86	34.05	39.57	50.77	56.09	57.13

resulting in the formation of the characteristic layered, puckered structure of BP. The progressive evolution of morphology, confirmed by SEM and TEM, shows a clear transition from amorphous agglomerated RP particles to well-defined layered structures emerging at 160–200 °C. At 200 °C, the disappearance of one of the peaks marked with a hash (#) indicates the emergence of a pure orthorhombic BP structure. The observed additional peaks (#) can be ascribed to the replacement of two phosphorus atoms with either oxygen or hydrogen, as well as periodic distortions or stacking faults along the *c*-axis.[33,37] This interpretation is confirmed by energy dispersive X-ray (EDX) analysis, which has effectively eliminated the possibility of impurities being present. The obtained orthorhombic phase has Miller indices corresponding to Bragg angles, as shown in Table 1.

Using Bragg's law,

$$n\lambda = 2d_{hkl}\sin\theta \qquad (1)$$

and the lattice plane spacing equation,

$$d_{hkl} = \frac{1}{\sqrt{\frac{h^2}{a^2} + \frac{k^2}{b^2} + \frac{l^2}{c^2}}} \qquad (2)$$

We determined the lattice parameters of BP-200.[39] The calculated values are summarized in Table 2.

The determined lattice parameters exhibit a strong correlation with the values documented in the JCPDS reference file (No. 073-1358), with slight discrepancies ascribed to the strain present in the synthesised nanostructures.[40] The strain is additionally supported by the Williamson–Hall (WH) plot, illustrated in Fig. 2(b and c). The Williamson–Hall plot serves as a graphical representation of the Williamson–Hall equation:

$$\beta\cos\theta = \varepsilon(4\sin\theta) + \frac{k\lambda}{D} \qquad (3)$$

In this context, *k* is defined as a constant, while λ is 1.5406 Å, which corresponds to the wavelength of the employed X-ray source. The term *β* refers to the full width at half maximum (FWHM), *ε* signifies the strain present in the material, and *D* (nm) indicates the crystallite size.[41] The WH equation offers a valuable insight into the strain and crystallite size of the material.

Table 2 Lattice parameters of BP-200 compared with JCPDS reference values

Lattice parameter	Calculated	JCPDS (073-1358)
a (Å)	3.311	3.313
b (Å)	10.421	10.478
c (Å)	4.373	4.376

4.2. Raman spectra analysis

Raman spectroscopy functions as an essential instrument for evaluating the crystallinity of synthesised phases and nanostructures. Fig. 3 illustrates the Raman spectra. The Raman spectra indicate that at an initial synthesis temperature of 120 °C, the predominant Raman modes are associated with black phosphorus in the wavenumber range of 300–600 cm^{-1} with the most prominent peak at 468.56 cm^{-1}, while the less intense peaks can be ascribed to residual RP. In the case of BP-140, the Raman peaks corresponding to RP diminish significantly. With each increment of 20 °C in temperature, solely the Raman peaks associated with BP are detected, signifying a complete phase transition. The peak identified as P–O at approximately 393.31 cm^{-1} is associated with the oxidation process of the synthesised BP.[33] Moreover, the crystallinity of the synthesised samples exhibits enhancement as the temperature rises. The observed Raman modes substantiate the transition from RP to BP,[21,42] alongside the elevated crystallinity of BP-200, aligning with the findings from the XRD analysis. Table 3 presents the characteristic Raman modes along with their respective wavenumbers for RP and BP-200.

Although the Raman spectra were discussed, we now provide a detailed correlation between the observed spectral features and crystallinity. Specifically, the BP-200 exhibited a
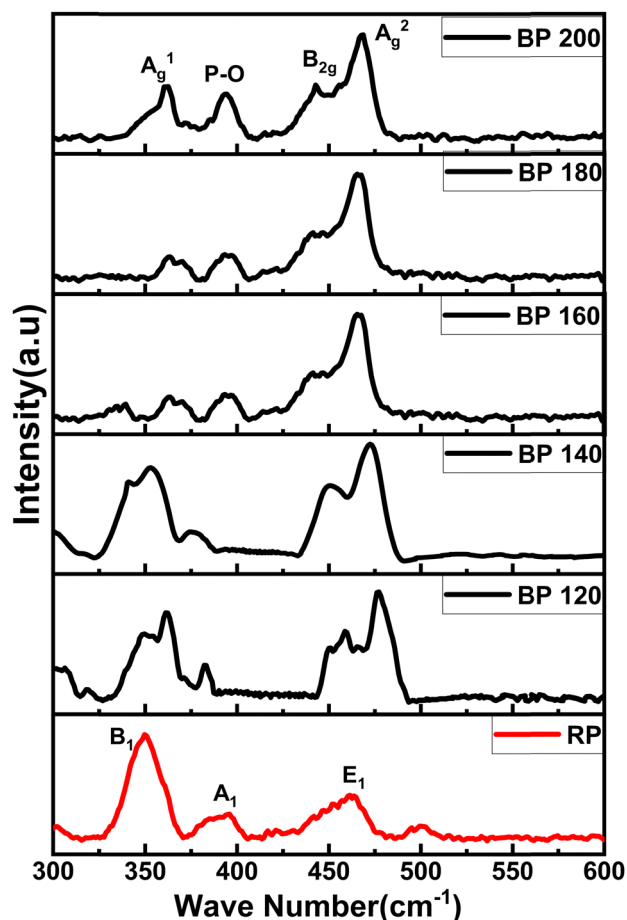
Fig. 3 Raman spectra of RP, BP-120, BP-140, BP-160, BP-180 and BP-200.

Table 3 Characteristic Raman modes and wavenumbers for RP and BP-200

Raman mode	RP wavenumber (cm^{-1})	BP-200 wavenumber (cm^{-1})
B_1	350.16	—
A_1	395.31	—
E_1	462.62	—
A_g^1	—	361.62
B_g^2	—	443.22
A_g^2	—	468.56
P–O		393.31

noticeable increase in peak intensity along with reduced FWHM values for all three modes, compared to BP/RP hybrids as shown in Table 4. These observations indicate enhanced crystallinity, reduced structural defects, and improved layer ordering in the BP/RP hybrid, consistent with literature reports where sharper, more intense Raman peaks reflect superior crystalline quality and fewer lattice distortions.[43]

4.3. Transmission electron microscopy (TEM) and selected area electron diffraction (SAED) analysis of the synthesized black phosphorus

Transmission electron microscopy (TEM) and high-resolution TEM (HR-TEM) offer profound insights into the morphology, structural characteristics, and crystallinity of the synthesised black phosphorus (BP). Fig. 4 illustrates the TEM and HR-TEM images, accompanied by the selected area electron diffraction (SAED) patterns. The transmission electron microscopy images illustrate an agglomerated sheet-like morphology characteristic of black phosphorus nanostructures,[44] thereby confirming the exfoliated nature of the synthesised material.[42] The selected area electron diffraction (SAED) pattern illustrated in Fig. 4(e) provides additional evidence supporting the crystallinity of the synthesised black phosphorus (BP). The indexing of the diffraction spots corresponds to the (021), (111), and (151) planes, aligning with the orthorhombic crystal structure confirmed by the JCPDS reference file (No. 073-1358). The observation of well-defined and distinct diffraction spots signifies a high degree of crystallinity in the synthesised material. The HR-TEM image depicted in Fig. 4(d) provides a detailed examination of the atomic structure, clearly revealing well-defined lattice fringes corresponding to the (111), (151) and (060) planes. The measured interplanar spacings of 0.245 nm for the (111) plane, 0.166 nm for the (151) plane and 0.176 nm for (060) plane are in excellent agreement with the theoretical values for black phosphorus.[45] Furthermore, the inverse FFT plot profile

(Fig. 4e) elucidates the intensity fluctuations across the lattice fringes, thereby offering additional validation of the periodic atomic configuration and the structural robustness of the synthesised black phosphorus.

4.5. Morphological and compositional characterization analysis
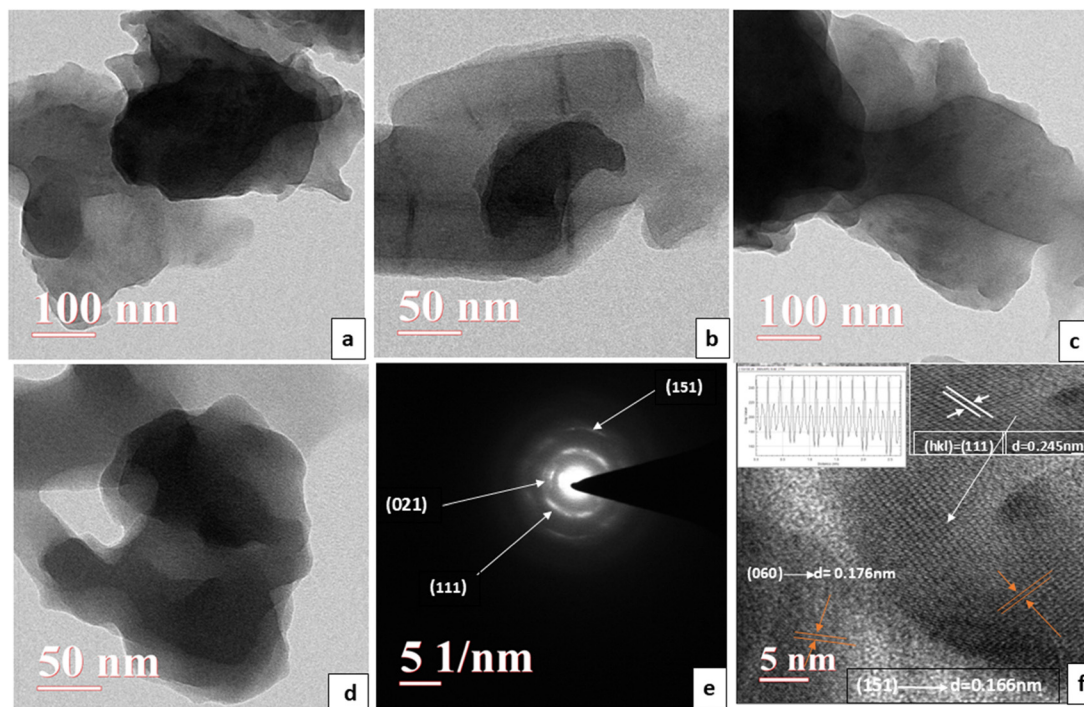
4.5.1. Scanning electron microscopy (SEM) and energy dispersive X-ray spectroscopy (EDX) analysis. The application of scanning electron microscopy (SEM) and energy dispersive X-ray (EDX) spectroscopy yields critical information regarding the surface morphology, microstructure, and elemental composition of black phosphorus (BP) synthesised under varying thermal conditions. Fig. 5 illustrates the SEM and EDX images. The SEM analysis elucidates the morphological changes of black phosphorus as the synthesis temperature is elevated. The RP microstructure (Fig. 5a) exhibits an irregular morphology and a rough surface texture, which are reflective of its amorphous characteristics. At 160 °C (Fig. 5(b)), the transition to BP initiates, accompanied by the appearance of layered characteristics. At 180 °C (Fig. 5c), the layers exhibit increased uniformity and organisation, signifying the prevalence of the orthorhombic phase. The magnified SEM image of BP synthesised at 200 °C (Fig. 5(d)) reveals well-exfoliated and distinctly defined layers, whereas Fig. 5(e) emphasises the hierarchical arrangement of these layers. The EDX spectrum presented in Fig. 5f serves to validate the purity of BP synthesised at a temperature of 200 °C. The prominent phosphorus peak confirms the effective synthesis of black phosphorus, whereas the lesser peaks of oxygen and carbon are probably due to surface oxidation as evidenced by Raman spectra and XPS spectra.

4.5.2. X-ray photoelectron spectroscopy analysis. The investigation of the surface structure and chemical environment of phosphorus molecules within the as-prepared black phosphorus nanosheets is conducted using X-ray photoelectron spectroscopy (XPS). The detailed scanning XPS spectra are illustrated in Fig. 6. The results of the fitting analysis indicate that the P 2p spectrum displays distinct peaks at approximately 130 eV ($2p_{3/2}$) and around 132 eV ($2p_{1/2}$), which are indicative of elemental phosphorus (P°) present in black phosphorus.[32] A secondary peak observed at approximately 134 eV is associated with P_2O_5, suggesting the occurrence of partial surface oxidation.[46] The O 1s spectrum reveals two prominent peaks at approximately 531.5 eV (O=P) and around 533 eV (O–P), thereby substantiating the occurrence of surface oxidation as a result of environmental exposure.[47] The C 1s spectrum displays a prominent peak at approximately 284 eV, which is

Table 4 Comparison of Raman peak positions, FWHM, and intensities for different samples

| Sample	Wave numbers of A_g^1 mode (cm^{-1})	FWHM A_g^1 (rad.)	Intensity A_g^1 (a.u.)	Wave numbers of B_{2g} mode (cm^{-1})	FWHM B_{2g} (rad.)	Intensity B_{2g} (a.u.)	Wave numbers of A_g^2 mode (cm^{-1})	FWHM A_g^2 (rad.)	Intensity A_g^2 (a.u.)
BP-120 °C	362.0	12.5	75	444.1	13.8	62	469.0	12.9	58
BP-140 °C	361.8	10.3	95	443.5	11.7	88	468.7	11.1	85
BP-160 °C	361.7	9.2	110	443.3	10.6	105	468.6	9.9	98
BP-1800 °C	361.6	8.5	120	443.2	9.8	115	468.5	9.2	110
BP-200 °C	361.5	7.4	135	443.1	8.6	130	468.4	8.0	125

Fig. 4 (a)–(d) TEM pictures of BP-200 and the BP/RP hybrid at 100 nm and 50 nm resolutions. (e) BP-200 SAED pattern showing the (021), (111), and (151) plane indexed diffraction spots. (f) HR-TEM image of the lattice fringes with 0.245 nm, 0.166 nm and 0.176 interplanar spacings, corresponding to the (111) (060) and (151) respective crystallographic plane, with the inverse FFT plot profile exhibiting intensity changes.

ascribed to adventitious carbon contamination. Additionally, there are peaks observed at around 286 eV (P–N) and 285 eV (P–P), suggesting the presence of chemical interactions that involve phosphorus.[48] The N 1s spectrum exhibits a significant peak at approximately 399 eV, indicative of N–P bonding, alongside a lesser peak at around 400 eV, associated with C–N bonding.[13] While the oxidation of the as-prepared black phosphorus nanosheets is an unavoidable process, it has been documented that this oxidation can enhance the stability of BP nanosheets.[32]

4.6. Brunauer–Emmett–Teller (BET) analysis

Fig. 7 illustrates the N_2 absorption and desorption isotherms for BP-200, RP, and RP/BP hybrids. Upon examining the curves, a comparison of the specific surface area calculated by the
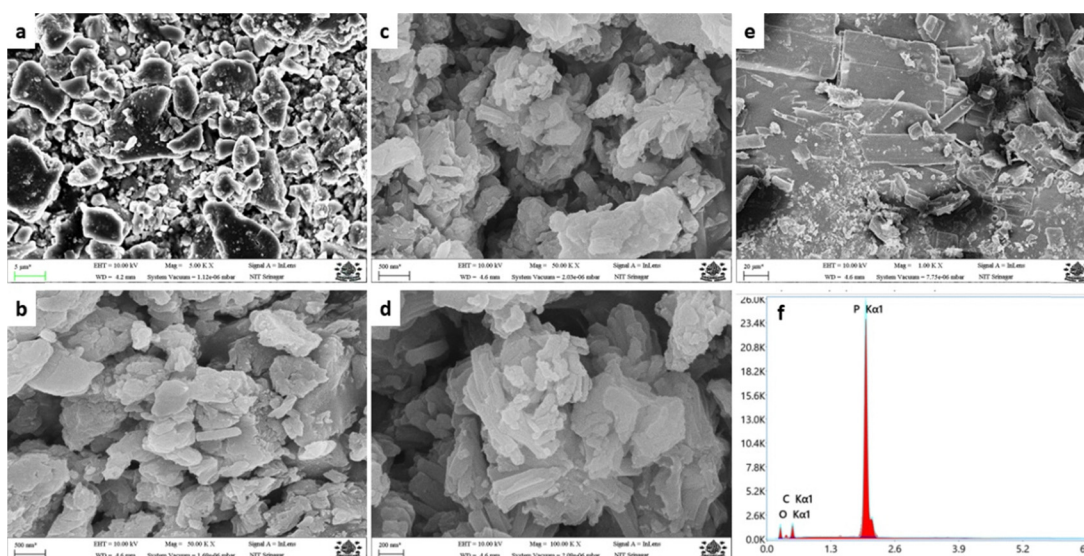
Fig. 5 (a) RP SEM picture exhibiting irregular microstructures without layers. (b) SEM picture of BP-160 BP showing multilayer structures. (c) SEM picture of BP-180 showing enhanced layer consistency and stacking. (d) SEM picture of BP-200 showing layer hierarchy. (e) Magnified SEM picture of BP-200 with well-defined exfoliated layers. (f) EDX of BP-200.
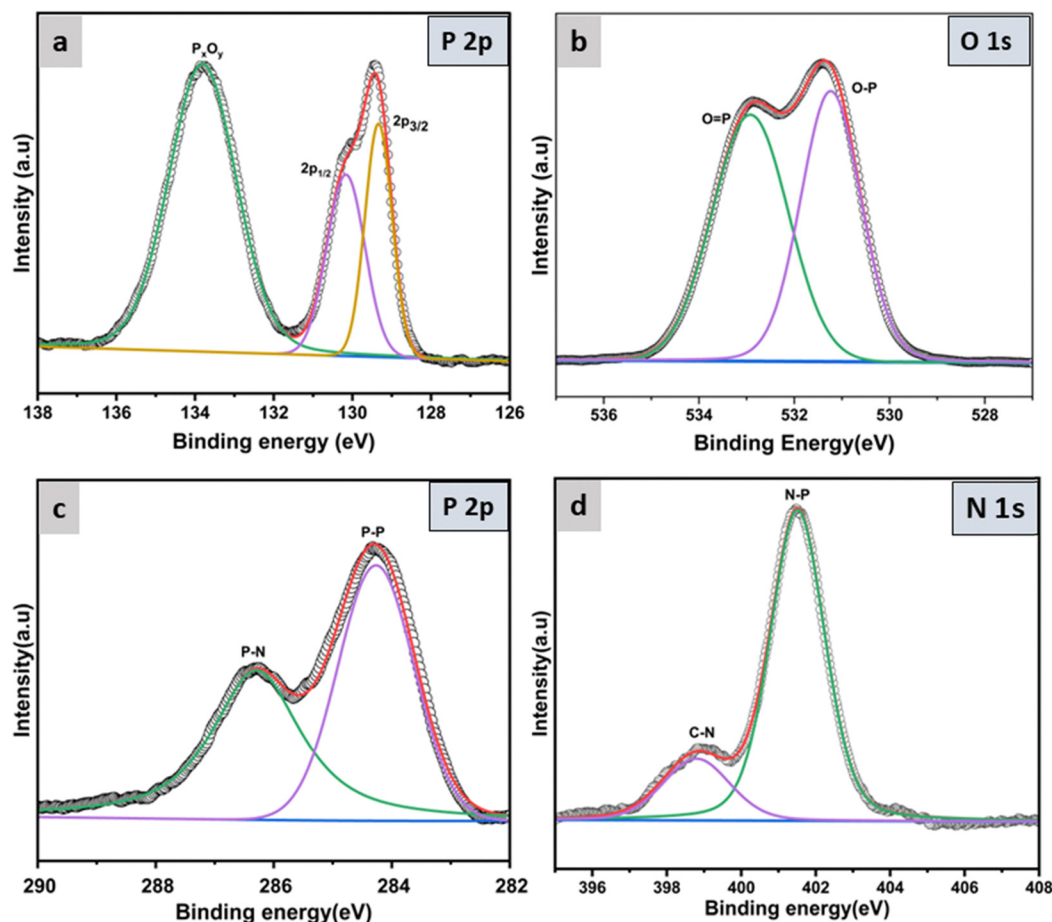
Fig. 6 (a) High-resolution XPS spectrum of BP-200 with P 2p peaks corresponding to P_2O_5 (oxidized phosphorus) and $P°$ (elemental phosphorus). (b) O 1s spectrum showing contributions from O=P and O–P bonds, indicative of surface oxidation. (c) C 1s spectrum with peaks corresponding to P–N and P–P bonding. (d) N 1s spectrum highlighting N–P and C–N bonding.

Brunauer–Emmett–Teller (BET) method can be conducted.[49] The calculated Brunauer–Emmett–Teller (BET) surface areas for RP and BP-200 are 3.86 $m^2 \, g^{-1}$ and 16.27 $m^2 \, g^{-1}$, respectively, whereas the RP/BP sample exhibits a surface area of 29.30 $m^2 \, g^{-1}$. The specific surface area of the RP/BP hybrid surpasses that of both pristine BP-200 and sole RP. This elevated specific surface area enhances the availability of reactive sites within the active materials, thereby augmenting the contact area between these materials and the electrolyte ions.[24] This phenomenon contributes to an improved reaction efficiency in the context of energy storage processes as revealed by electrochemical characterizations of the hybrid.

4.7. Electrochemical analysis

The electrochemical properties of red phosphorus (RP), black phosphorus (BP-200), and the BP/RP hybrid were thoroughly investigated using cyclic voltammetry (CV), galvanostatic charge–discharge (GCD), and electrochemical impedance spectroscopy (EIS).

Working electrodes were prepared by coating a slurry of 80 mg active material, 10 mg carbon black (conductive agent), and 10 mg polyvinylidene fluoride (PVDF, binder) in an

8 : 1 : 1 (wt%) ratio onto carbon electrodes (geometric area: 2 cm × 0.5 cm) using N-methyl pyrrolidinone (NMP) as the solvent. Approximately 1–2 mg of active material was uniformly distributed on each electrode. Electrochemical measurements were conducted using a Bio-Logic SP-200 workstation with a 1 M KOH aqueous electrolyte at room temperature. A standard three-electrode configuration was employed, with an Ag/AgCl reference electrode and a platinum (Pt) sheet counter electrode. The voltage range for testing was set between −4 V and 4 V.

4.7.1. Cyclic voltammetry (CV) analysis. Fig. 8(a) displays the CV curves of the BP/RP hybrid at scan rates ranging from 5 mV s^{-1} to 50 mV s^{-1}. The quasi-rectangular shape of the CV curves suggests a combination of electric double-layer capacitance (EDLC) and faradaic charge storage mechanisms, indicative of pseudocapacitive behaviour.[25] The minimal distortion of the curves at increasing scan rates highlights the excellent rate capability and power performance of the BP/RP hybrid.[50] Notably, the BP/RP hybrid maintained superior capacitance even at high scan rates, a critical attribute for efficient energy storage applications. In contrast, the CV curves of pristine BP-200 and RP exhibited a more rectangular shape, dominated
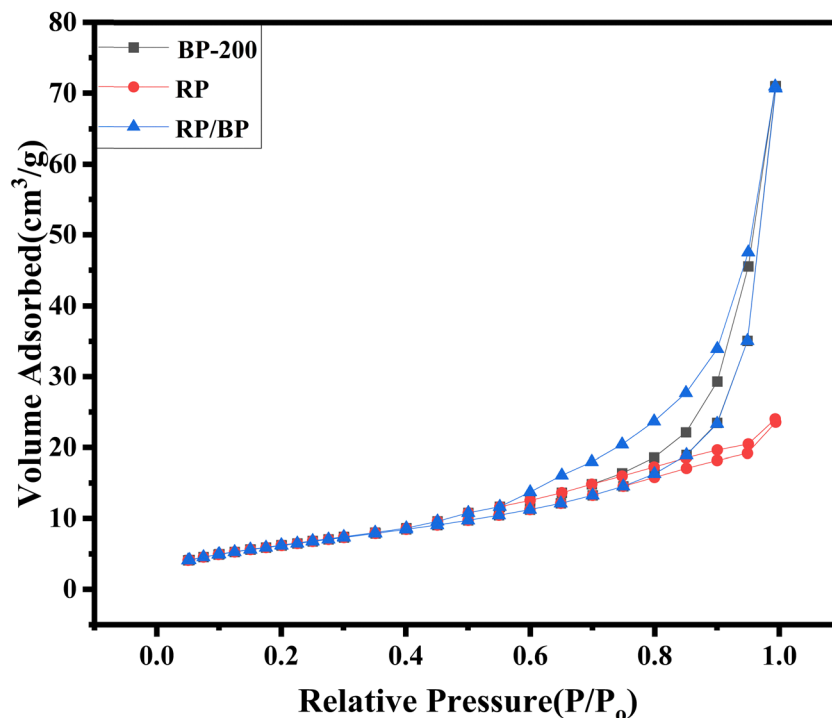
Fig. 7 N$_2$ absorption/desorption isotherm for the BP-200, RP, and RP/BP hybrids.

by EDLC behaviour with minimal faradaic contributions.[3] The slight deviation from ideal rectangular shapes in the CV curves is attributed to the irreversible reaction between phosphorus and water.[25]

4.7.2. Galvanostatic charge–discharge (GCD) analysis. The GCD profiles of the BP/RP hybrid, BP-200, and RP at various current densities are presented in Fig. 8(d–f). At low current densities, the charge–discharge curves deviated from the ideal
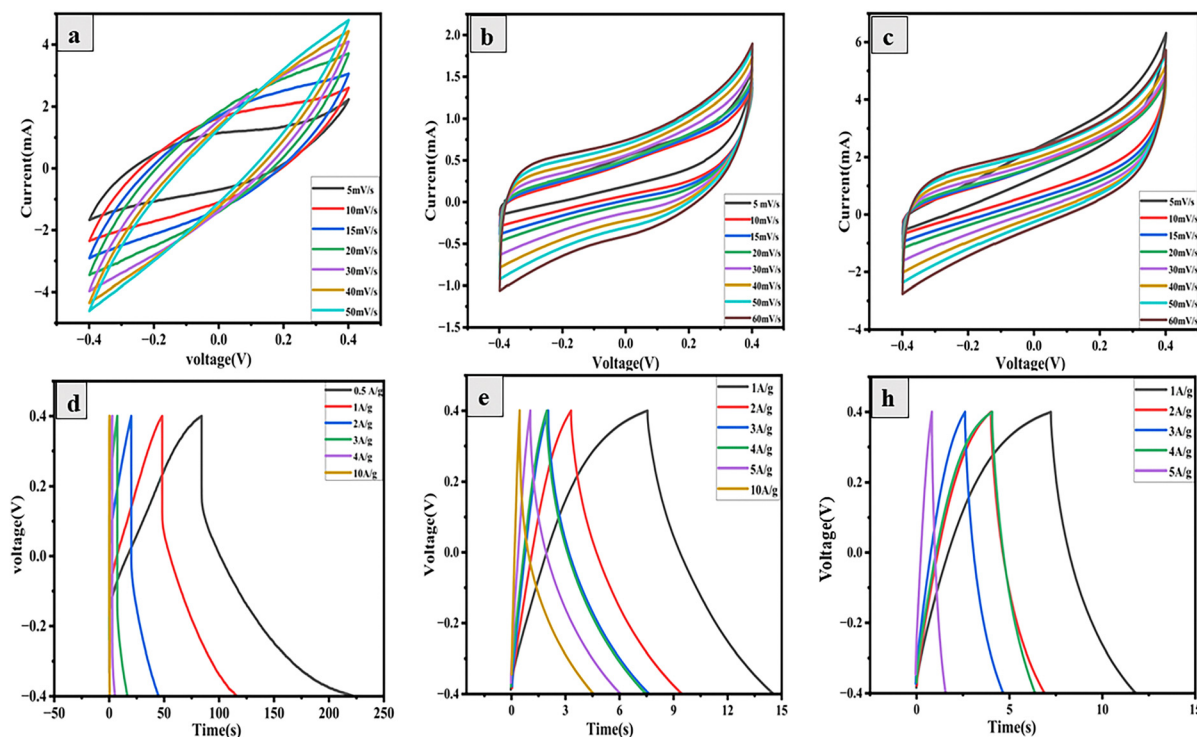

Fig. 8 (a) and (d), (b) and (e) and (c) and (f) are CV and GCD curves of the BP/RP hybrid, BP-200 and RP respectively.

linear slope, reflecting the coexistence of faradaic and non-faradaic charge storage mechanisms.[51] At higher current densities, the curves adopted a more triangular shape, consistent with EDLC behaviour.[52,53] The specific capacitance (C_s) was calculated using the equation:

$$C_s = \frac{I\Delta t}{m\Delta V} \tag{4}$$

where I is the discharge current, Δt is the discharge time, m is the mass of the active material and ΔV is the potential window. The BP/RP hybrid demonstrated specific capacitances of 87 F g^{-1}, 69 F g^{-1}, and 62.5 F g^{-1} at current densities of 0.5 A g^{-1}, 1 A g^{-1}, and 2 A g^{-1}, respectively. These values significantly exceed

those reported for phosphorus-based composites in previous studies, as summarized in Table 5, including pristine BP (9 F g^{-1} at 1 A g^{-1}) and RP (6 F g^{-1} at 1 A g^{-1}), highlighting the superior electrochemical performance of the RP/BP hybrid material. The decline in capacitance at higher current densities is attributed to diffusion limitations and electrode overpotential, which restrict ion transport to the electrode surface.[54,55]

4.7.3. Electrochemical impedance spectroscopy (EIS) analysis. To investigate the electrode kinetics of the BP/RP hybrid, BP, and RP, electrochemical impedance spectroscopy (EIS) was conducted. As illustrated in the Nyquist plot (Fig. 9c), the impedance response comprises three distinct regions: (1) a high-frequency intercept corresponding to ohmic resistance, attributed to the combined resistance of the electrolyte and electrical contacts. The extracted R_s values are 0.82 Ω for the RP/BP Hybrid, 2.2 Ω for BP-200 and 4.3 Ω for RP electrodes.[57] The extracted R_s values fall within the expected range for aqueous electrolyte systems as reported in the literature. Minor deviations may stem from cell geometry (*e.g.*, electrode spacing) or instrumental factors.[58] (2) A depressed semicircle in the mid-frequency range, representing the charge-transfer resistance (R_{ct}) and ion migration resistance through the solid electrolyte interphase (SEI) layer; and (3) an inclined Warburg tail at low frequencies, indicative of solid-state potassium diffusion.[59,60] The equivalent circuit model of the test system is

Table 5 Comparison of specific capacitance for phosphorus-based nanostructures

S. no.	Material system	Electrolyte	Current density (A g^{-1})	Specific capacitance (F g^{-1})	Ref.
i	BP nanoflakes	PVA/H$_3$PO$_4$	0.5	48.8	25
ii	RP/BP hybrid	1 M KOH	0.5	60.1	50
iii	RGO/BP film	1 M H$_3$PO$_4$	0.25	104	56
iv	**BP/RP hybrid**	1 M KOH	0.5	**87**	Present work
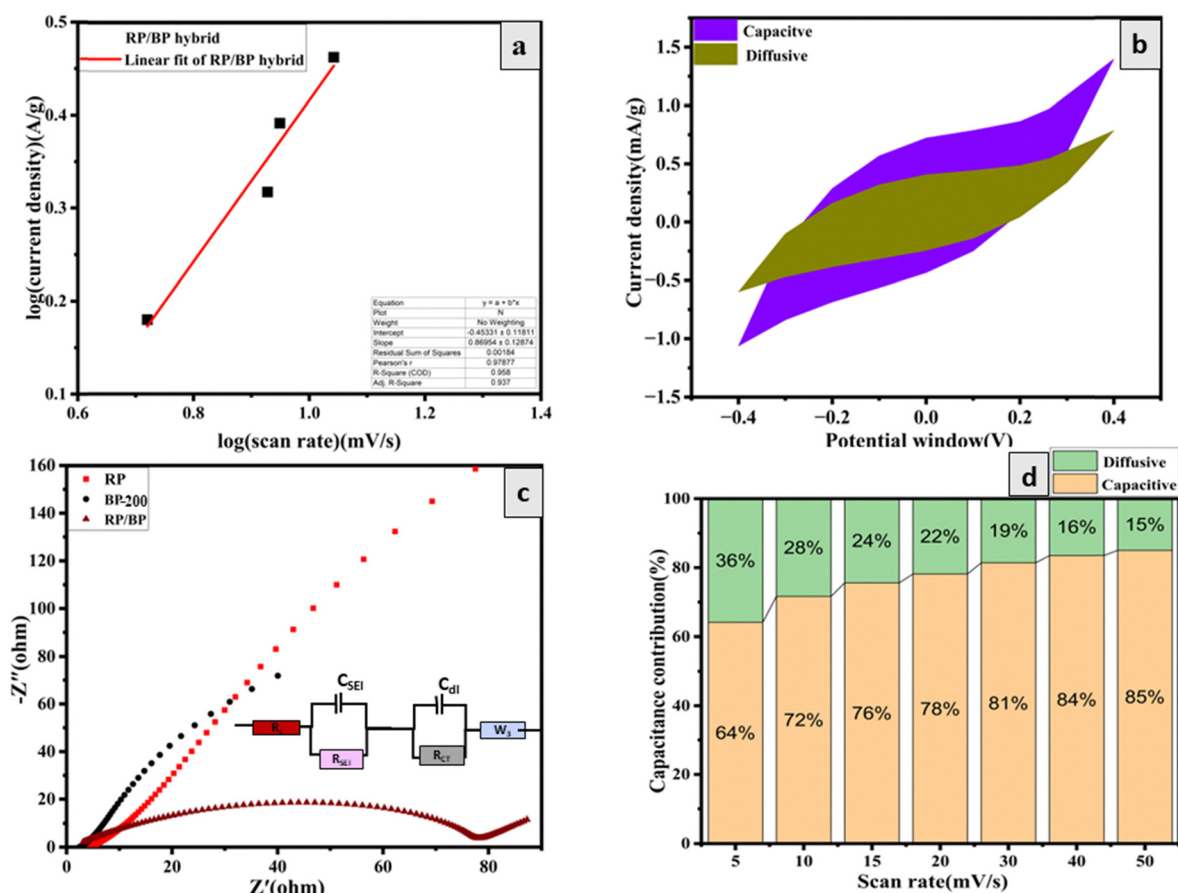
Fig. 9 (a) Linear fit for "*b*" value. (b) Capacitance contribution analysis in the RP/BP hybrid *via* CV at 0.5 mV s^{-1}. (c) Nyquist plots of RP, BP, and the RP/BP hybrid with Randles circuit. (d) Capacitance contribution in the RP/BP hybrid using the Dunn method.

shown in the inset of Fig. 9(c). Analysis of the circuit indicates that the interfacial resistance (R_f) follows the order RP (83 Ω) > BP (54 Ω) > BP/RP (31 Ω), demonstrating that the BP/RP hybrid forms a more stable surface film compared to RP.[34] Additionally, the charge transfer resistance (R_{ct}) of BP/RP (91 Ω) is lower than that of BP-200 (127 Ω) and RP (475 Ω), highlighting enhanced electron transfer and fast ion diffusion in the BP/RP electrode.[61] The EIS analysis confirms the hypothesis that the BP/RP electrode exhibits superior electrical conductivity and enhanced charge-transfer capabilities compared to the pristine BP-200 and individual RP electrodes.

Fig. 10 illustrates the Bode plot representations derived from the EIS data. Bode plot representations of phase angle (ϕ) as a function of frequency serve as a tool to illustrate the relative contributions of capacitive and resistive elements, with ideal capacitance positioned at $\phi = 90$, while resistive processes (such as the conduction of electrons across and through the electrode and diffusion limitations linked to battery-like reactions) are represented by $\phi = 0$.[62,63] The response observed through electrochemical impedance spectroscopy (EIS), as illustrated in the Bode plots, showcases charge storage characteristics for RP, BP, and the RP/BP hybrid electrodes. The Bode plots reveal that RP/BP demonstrates a more pronounced phase angle nearing $-80°$ at lower frequencies when compared to pristine RP and BP, suggesting enhanced capacitive performance with diminished resistive effects. The impedance modulus ($|Z|$) for RP/BP consistently shows lower values throughout the frequency range, indicating improved ionic conductivity and reduced charge transfer resistance. The RP/BP hybrid showcases an impressive frequency bandwidth along with a stable phase response, indicating effective ion diffusion and enhanced electrochemical kinetics. The Nyquist plots (Fig. 9d) further substantiate these findings, showcasing the RP/BP hybrid's smaller semicircular arc in the high-frequency region and a steeper, almost vertical line in the low-frequency domain, indicative of capacitive behaviour. The diminished charge-transfer resistance and enhanced Warburg diffusion suggest collaborative effects between RP and BP, optimising ion transport routes and enabling swift electrochemical reactions. The enhancements in impedance characteristics demonstrate that the hybrid structure effectively merges the pseudocapacitive attributes with the conductivity improvements, resulting in superior performance by facilitating rapid ion and electron transport along with increased energy storage efficiency. In electrochemical systems,

the total capacitance of an electrode arises from two distinct contributions.[55] The first component involves rapid electrochemical processes, such as faradaic reactions (e.g., redox reactions) and ion adsorption/desorption at the electrode surface, commonly referred to as electric double-layer capacitance (EDLC). The second component is governed by diffusion-controlled processes, where ion transport occurs within the electrode material and the electrolyte. To evaluate the performance of electrode materials effectively, it is crucial to identify the dominant mechanism driving the electrochemical behaviour. Surface-controlled processes, including EDLC and faradaic reactions, can be distinguished from diffusion-controlled processes in charge storage mechanisms using the power-law relationship.

$$I = av^b \tag{5}$$

where I signifies the current density, v indicates the scan rate, and a and b are parameters that can be adjusted. In general, the gradient of the logarithmic representation of current (I) *versus* the logarithm of the scan rate (v) at a specific potential provides the b-value. A b-value nearing 1 signifies a process governed by surface control and capacitance, while a b-value around 0.5 implies that the process is dominated by diffusion mechanisms. In the case of the RP/BP hybrid, the b-value of 0.87, as illustrated in Fig. 9(a), suggests that the charge storage mechanism is predominantly influenced by a surface-controlled capacitive process.[64]

In order to enhance the quantification of surface capacitive effects alongside diffusion-controlled phenomena, Dunn's equation[65] was utilised:

$$I(v) = k_1 v + k_1 v^{1/2} \tag{6}$$

In this analysis, $I(v)$ represents the current response at a specific potential, v denotes the scan rate, and k_1 and k_2 are constants determined from the slope and intercept of the linear relationship between $I(v)/v^{1/2}$ and $v^{1/2}$, respectively. For the BP/RP hybrid electrode at a scan rate of 5 mV s^{-1}, surface-controlled processes, represented by the shaded blue regions in Fig. 9(b), account for 68% of the total charge storage capacity. Fig. 9(d) further illustrates that the capacitive contribution increases with higher scan rates. These findings underscore the complex interplay between electrochemical kinetics and the capacitive behaviour of the electrode.
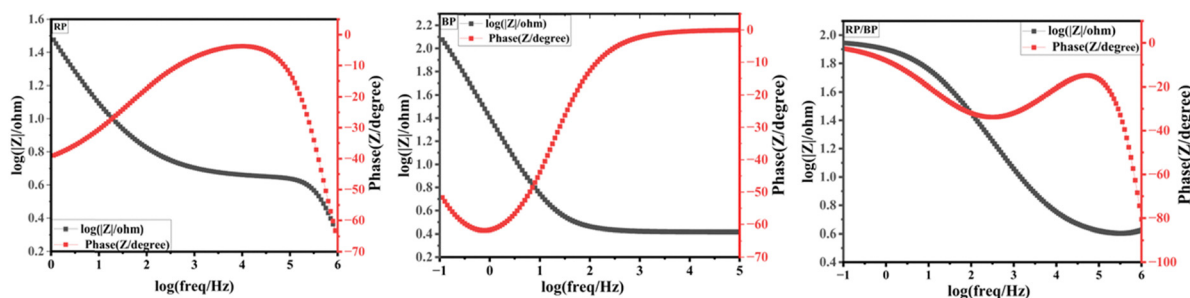

Fig. 10 Bode plots of the RP, BP, and RP/BP electrodes, respectively.

5. Conclusion

The systematic investigation of black phosphorus (BP) and red phosphorus/black phosphorus (RP/BP) hybrids revealed a successful solvothermal phase transition from amorphous RP to crystalline orthorhombic BP, as confirmed by XRD and Raman spectroscopy. Structural and morphological analysis through Raman spectra reveals distinct BP modes at 361.62 cm^{-1} (A_g^1), 443.22 cm^{-1} (B_{2g}), and 468.56 cm^{-1} (A_g^2). Transmission electron microscopy and selected area electron diffraction validated the crystalline characteristics of BP, revealing lattice fringes that align with the (111), (151) and (060) planes, with respective interplanar spacings of 0.245 nm, 0.166 nm and 0.176 nm, while BET measurements demonstrated an enhanced specific surface area (29.30 m^2 g^{-1}) for the BP/RP hybrid compared to pristine BP-200 (16.27 m^2 g^{-1}) and RP (3.86 m^2 g^{-1}). Electrochemical characterizations through cyclic voltammetry, galvanostatic charge/discharge and electron impedance spectroscopy highlighted the hybrid's superior pseudocapacitive performance, achieving a specific capacitance of 87 F g^{-1} at 0.5 A g^{-1}, surpassing previous reports, with charge transfer resistance (R_{ct}) of BP/RP (91 Ω) lower than that of BP-200 (127 Ω) and RP (475 Ω), highlighting enhanced electron transfer and fast ion diffusion in the BP/RP electrode. These findings underscore the potential of BP/RP hybrids as advanced electrode materials for high-performance supercapacitors, leveraging their optimized structural and electrochemical aspects.

Author contributions

Shahbaz Ahmad: conceptualization, data curation, formal analysis, investigation, methodology, software, validation, visualization, writing – original draft, writing – review & editing. Mohd Zubair Ansari: review & editing, resources, supervision.

Conflicts of interest

The work described in this article could not have been influenced by the author's known conflicting financial interests or personal ties.

Data availability

This article contains all the data created or examined during this investigation.

Acknowledgements

References

1 P. Simon and Y. Gogotsi, *Nat. Mater.*, 2008, **7**, 845.
2 M. Xu, T. Liang, M. Shi and H. Chen, *Chem. Rev.*, 2013, **113**, 3766.
3 J. C. Ellenbogen, *Supercapacitors: A Brief Overview*, 2006, p. 41.
4 T. Wang, K. Li, Q. Le, S. Zhu, X. Guo, D. Jiang and Y. Zhang, *J. Colloid Interface Sci.*, 2021, **594**, 812.
5 K. Li, Z. Guo, Q. Sun, X. Dai, Y. Li, K. Yao, X. Liu, Z. Bao, J. Rao and Y. Zhang, *Chem. Eng. J.*, 2023, **454**, 140223.
6 K. Li, H. Teng, Q. Sun, Y. Li, X. Wu, X. Dai, Y. Wang, S. Wang, Y. Zhang, K. Yao, Z. Bao, J. Rao and Y. Zhang, *J. Energy Storage*, 2022, **53**, 105094.
7 K. Li, C. Yin, X. Dai, J. Zhang, S. Yi, J. Rao and Y. Zhang, *J. Energy Storage*, 2022, **55**, 105722.
8 K. Li, Y. Xiao, T. Zheng, Q. Sun, Y. Zhang, H. Teng, W. Wang, K. Yao, J. Rao and Y. Zhang, *Appl. Surf. Sci.*, 2023, **622**, 156950.
9 Z. S. Wu, K. Parvez, X. Feng and K. Müllen, *Nat. Commun.*, 2013, 4, DOI: **10.1038/ncomms3487**.
10 H. Kelly-Holmes, *Advertising as Multilingual Communication*, 2016, vol. 45, p. 1.
11 S. Das, W. Zhang, M. Demarteau, A. Hoffmann, M. Dubey and A. Roelofs, *Nano Lett.*, 2014, **14**, 5733.
12 Y. Yang, J. Gao, Z. Zhang, S. Xiao, H. H. Xie, Z. B. Sun, J. H. Wang, C. H. Zhou, Y. W. Wang, X. Y. Guo, P. K. Chu and X. F. Yu, *Adv. Mater.*, 2016, **28**, 8937.
13 Y. Wang, M. He, S. Ma, C. Yang, M. Yu, G. Yin and P. Zuo, *J. Phys. Chem. Lett.*, 2020, **11**, 2708.
14 S. Zhu, Q. Liang, Y. Xu, H. Fu and X. Xiao, *Eur. J. Inorg. Chem.*, 2020, 773.
15 Y. Yi, Z. Sun, J. Li, P. K. Chu and X. F. Yu, *Small Methods*, 2019, **3**, 1.
16 S. A. Ansari and M. H. Cho, *Sci. Rep.*, 2016, **6**, 1.
17 N. Sultana, A. Degg, S. Upadhyaya, T. Nilges and N. Sen Sarma, *Mater. Adv.*, 2022, **3**, 5557.
18 Z. K. Shen, Y. J. Yuan, L. Pei, Z. T. Yu and Z. Zou, *Chem. Eng. J.*, 2020, **386**, 123997.
19 J. O. Island, G. A. Steele, H. S. J. Van Der Zant, A. Castellanos-Gomez, J. D. Wood, S. A. Wells, D. Jariwala, K. Chen, E. Cho, V. K. Sangwan, X. Liu, L. J. Lauhon, T. J. Marks and M. C. Hersam, *Nano Lett.*, 2014, **14**, 6964.
20 M. Mayo, K. J. Griffith, C. J. Pickard and A. J. Morris, *Chem. Mater.*, 2016, **28**, 2011.
21 S. H. Aldave, M. N. Yogeesh, W. Zhu, J. Kim and S. S. Sonde, *2D Mater.*, 2019, **3**, 491–498.
22 L. Q. Sun, M. J. Li, K. Sun, S. H. Yu, R. S. Wang and H. M. Xie, *J. Phys. Chem. C*, 2012, **116**, 14772.
23 C. M. Park and H. J. Sohn, *Adv. Mater.*, 2007, **19**, 2465.
24 Y. Wu, W. Yuan, M. Xu, S. Bai, Y. Chen, Z. Tang, C. Wang, Y. Yang, X. Zhang, Y. Yuan, M. Chen, X. Zhang, B. Liu and L. Jiang, *Chem. Eng. J.*, 2021, **412**, 128744.

25 C. Hao, B. Yang, F. Wen, J. Xiang, L. Li, W. Wang, Z. Zeng, B. Xu, Z. Zhao, Z. Liu and Y. Tian, *Adv. Mater.*, 2016, **28**, 3194.

26 P. W. Bridgman, *J. Franklin Inst.*, 1915, **179**, 336.

27 S. Lange, P. Schmidt and T. Nilges, *Inorg. Chem.*, 2007, **46**, 4028.

28 J. Li, Z. Gao, X. Ke, Y. Lv, H. Zhang, W. Chen, W. Tian, H. Sun, S. Jiang, X. Zhou, T. Zuo, L. Xiao, M. Sui, S. Tong, D. Tang, B. Da, K. Yamaura, X. Tu, Y. Li, Y. Shi, J. Chen, B. Jin, L. Kang, W. Xu, H. Wang and P. Wu, *Small*, 2018, **14**, 1.

29 E. I. Jahre, D. Phosphor, W. Gunther, D. P. Stofidrucken, H. Krebs, H. Weitz and K. Worms, *J. Inorg. Chem.*, 1943, **280**, 119.

30 F. Zhou, L. Ouyang, M. Zeng, J. Liu, H. Wang, H. Shao and M. Zhu, *J. Alloys Compd.*, 2019, **784**, 339.

31 T. Bao, O. Tegus, Hasichaolu, J. Ning and Narengerile, *Solid State Phenom.*, 2018, **271 SSP**, 18.

32 B. Tian, B. Tian, B. Smith, M. C. Scott, Q. Lei, R. Hua, Y. Tian and Y. Liu, *Proc. Natl. Acad. Sci. U. S. A.*, 2018, **115**, 4345.

33 A. Ozawa, M. Yamamoto, T. Tanabe, S. Hosokawa and T. Yoshida, *J. Mater. Chem. A*, 2020, **8**, 7368.

34 X. Chen, G. Xu, X. Ren, Z. Li, X. Qi, K. Huang, H. Zhang, Z. Huang and J. Zhong, *J. Mater. Chem. A*, 2017, **5**, 6581.

35 F. Liu, R. Shi, Z. Wang, Y. Weng, C. Che and Y. Chen, *Angew. Chem.*, 2019, **131**, 11917.

36 C. Marino, L. Boulet, P. Gaveau, B. Fraisse and L. Monconduit, *J. Mater. Chem.*, 2012, **22**, 22713.

37 S. Radhakrishnan, N. Kuniyil, A. Sharma and C. S. Rout, *Energy Fuels*, 2023, **37**, 3196–3207.

38 J. Batur, Z. Duan, R. Jin, R. Li, Y. Xie, X. F. Yu and J. R. Li, *Inorg. Chem.*, 2024, **63**, 11860.

39 T. Ahmad and M. Z. Ansari, *Mater. Res. Express*, 2022, **9**, 105902.

40 T. Ahmad and M. Z. Ansari, *New J. Chem.*, 2024, **48**, 8495.

41 M. Zubair Ansari and N. Khare, *J. Appl. Phys.*, 2015, **117**, DOI: 10.1063/1.4905673.

42 V. Nicolosi, M. Chhowalla, M. G. Kanatzidis, M. S. Strano and J. N. Coleman, *Science*, 2013, **340**, DOI: 10.1126/science.1226419.

43 C. Wu, L. Jing, J. Deng, Y. Liu, S. Li, S. Lv, Y. Sun, Q. Zhang and H. Dai, *Chemosphere*, 2021, **274**, 129793.

44 X. Liu, J. D. Wood, K. S. Chen, E. Cho and M. C. Hersam, *J. Phys. Chem. Lett.*, 2015, **6**, 773.

45 A. Brown and S. Rundqvist, *Acta Crystallogr.*, 1965, **19**, 684.

46 M. T. Edmonds, A. Tadich, A. Carvalho, A. Ziletti, K. M. O'Donnell, S. P. Koenig, D. F. Coker, B. Özyilmaz, A. H. C. Neto and M. S. Fuhrer, *ACS Appl. Mater. Interfaces*, 2015, **7**, 14557–14562.

47 A. Favron, E. Gaufrès, F. Fossard, A. L. Phaneuf-Laheureux, N. Y. W. Tang, P. L. Lévesque, A. Loiseau, R. Leonelli, S. Francoeur and R. Martel, *Nat. Mater.*, 2015, **14**, 826.

48 M. T. Edmonds, A. Tadich, A. Carvalho, A. Ziletti, K. M. O'Donnell, S. P. Koenig, D. F. Coker, B. Özyilmaz, A. H. C. Neto and M. S. Fuhrer, *ACS Appl. Mater. Interfaces*, 2015, **7**, 14557.

49 Y. Zheng, Z. Yu, H. Ou, A. M. Asiri, Y. Chen and X. Wang, *Adv. Funct. Mater.*, 2018, 28, DOI: 10.1002/adfm.201705407.

50 X. Chen, G. Xu, X. Ren, Z. Li, X. Qi, K. Huang, H. Zhang, Z. Huang and J. Zhong, *J. Mater. Chem. A*, 2017, **5**, 6581.

51 X. Y. Fu, Z. Di Chen, Y. L. Zhang, D. D. Han, J. N. Ma, W. Wang, Z. R. Zhang, H. Xia and H. B. Sun, *Nanoscale*, 2019, **11**, 9133.

52 A. Sajedi-Moghaddam, C. C. Mayorga-Martinez, Z. Sofer, D. Bouša, E. Saievar-Iranizad and M. Pumera, *J. Phys. Chem. C*, 2017, **121**, 20532.

53 A. Rabiei Baboukani, I. Khakpour, V. Drozd, A. Allagui and C. Wang, *J. Mater. Chem. A*, 2019, **7**, 25548.

54 M. Aalim, U. Altaf, A. Rashid, R. Ahmad, A. Sohail, A. Mir and M. A. Shah, *J. Solid State Electrochem.*, 2024, **28**, 1.

55 S. Irfan, M. Aalim, M. H. Flaifel, I. Nazir, M. A. Shah, M. Q. Lone, A. Firdous, A. H. Pandith and G. N. Dar, *J. Energy Storage*, 2025, **106**, 114788.

56 J. Cao, P. He, J. R. Brent, H. Yilmaz, D. J. Lewis, I. A. Kinloch and B. Derby, *ACS Appl. Mater. Interfaces*, 2018, **10**, 10330.

57 W. Zhang, Z. Ren, Y. Guo, X. He and X. Li, *Electrochim. Acta*, 2018, **268**, 539.

58 F. Han, D. Li, W. C. Li, C. Lei, Q. Sun and A. H. Lu, *Adv. Funct. Mater.*, 2013, **23**, 1692–1700.

59 F. Han, D. Li, W. C. Li, C. Lei, Q. Sun and A. H. Lu, *Adv. Funct. Mater.*, 2013, **23**, 1692.

60 G. Sethi, B. Bontempo, E. Furman, M. W. Horn, M. T. Lanagan, S. S. N. Bharadwaja and J. Li, *J. Mater. Res.*, 2011, **26**, 745.

61 S. Zhang and N. Pan, *Adv. Energy Mater.*, 2015, **5**, 1.

62 J. S. Ko, M. B. Sassin, D. R. Rolison and J. W. Long, *Electrochim. Acta*, 2018, **275**, 225.

63 J. Huang, Z. Li, B. Y. Liaw and J. Zhang, *J. Power Sources*, 2016, **309**, 82.

64 M. Safari, J. Mazloom, K. Boustani and A. Monemdjou, *Sci. Rep.*, 2022, **12**, 1.

65 J. Wang, J. Polleux, J. Lim and B. Dunn, *J. Phys. Chem. C*, 2007, **111**, 14925.